J. Fluid Mech. (2007), *vol.* 592, *pp.* 51–78. © 2007 Cambridge University Press
doi:10.1017/S0022112007008300 Printed in the United Kingdom

Turbulent flow through a rectangular duct with a partially blocked exit

T. Y. HSU[1], H. ELORANTA[2], P. SAARENRINNE[2] AND T. WEI[1]

[1]Department of Mechanical, Aerospace & Nuclear Engineering, Rensselaer Polytechnic Institute, Troy, NY 12180-3590, USA

[2]Energy and Process Engineering, Tampere University of Technology, Tampere, Finland

(Received 4 August 2006 and in revised form 13 July 2007)

This paper contains data on and insights into the origins of turbulence associated with a partial blockage at the exit of a two-dimensional, laminar, horizontal duct flow. In essence, this is the upstream approach region of the forward-facing step problem. This work was motivated by the need to identify and control unsteady streamwise vortices generated in the headbox (i.e. contraction section) of an industrial paper machine. The duct was 57.2 cm wide × 10.16 cm high, with up to a 50 % blockage. Experiments were scaled to match Reynolds numbers found in paper machines; exit velocities were as large as 200 cm s^{-1}. The goal of the research was to map the flow at the exit and to examine the response of the flat-plate turbulent boundary layer on the opposing wall under the partial blockage. Laser-induced fluorescence (LIF) and digital particle image velocimetry (DPIV) were used to examine flow in three orthogonal planes at various stations upstream of the duct exit. Mean and instantaneous DPIV vector fields clearly show that an unsteady spanwise vortex forms in the corner formed by the top nozzle wall and partial blockage which, in turn, gives rise to turbulent streamwise vortices.

A turbulent boundary layer was initiated on the duct wall opposite the blockage, upstream of a two-dimensional contraction. Results show that even though the acceleration parameter, K, exceeded the nominal critical level of 3.0×10^{-6} for relaminarization beneath the blockage, the flow did not reach a quasi-laminar state. In addition, there did not appear to be direct interaction between unsteady vortex formation at the partial blockage on the upper wall and bottom-wall turbulent boundary layer structures.

1. Background and motivation

There are broad similarities between the front end of a paper machine and a fundamental two-dimensional jet flow facility. Both have a settling chamber, contraction and an exit nozzle. On a paper machine, these components are combined into what is referred to as a 'headbox'. However, whereas the jet flow facility is generally designed to minimize or eliminate turbulence upstream of the jet exit, the headbox is designed to *maximize* turbulence. Significant time and expense goes into designing turbulence generation devices along the entire flow path in the headbox. By maximizing turbulence, the paper maker hopes to keep wood fibres from flocculating, thereby minimizing or preventing formation of non-uniformities in the finished product.

https://doi.org/10.1017/S0022112007008300 Published online by Cambridge University Press

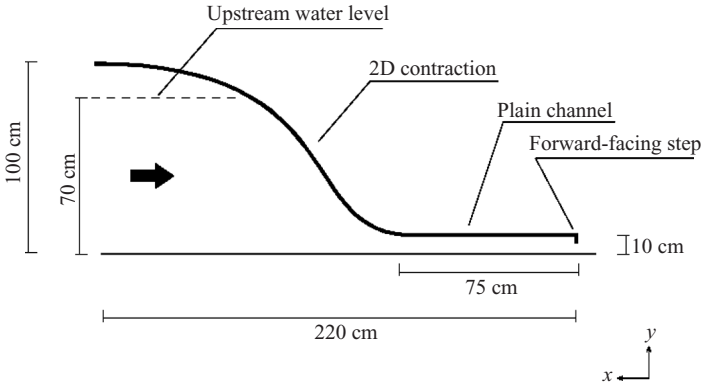


FIGURE 1. Side-view drawing of the variable cross-section channel including the laminar two-dimensional contraction, rectangular duct and partially blocked exit. Key dimensions, including the upstream water height are included. Note that for § 4, the y-direction is downward and the origin is located at the lower upstream corner of the partial blockage. For data presented in § 5, y is upward as shown and the origin is located on the bottom wall directly below the trailing face of the blockage.

Unfortunately, the same turbulence used to prevent flocculation also appears to produce it. Nonuniformities appear most frequently as elongated fibre 'flocs' aligned in the stream direction. These are known in the industry as 'streaks' or 'tiger stripes'. The origin of streaks is discussed in Soderberg & Alfredsson (1997) and Shah *et al.* (1999, 2000). Mechanisms postulated by Soderberg & Alfredsson (1997) include vortex stretching when flow accelerates through a two-dimensional nozzle; centrifugal instabilities associated with flow along a concave wall; and transition to turbulence of the headbox boundary layers.

By virtue of its design, it is problematic to use a headbox to decouple various hydrodynamics effects. Thus, it is virtually impossible to directly determine where paper streaks come from in an industrial setting. The research approach employed in this investigation was to deconstruct the headbox into a series of fundamental hydrodynamic models, or unit problems. The rationale was to isolate individual streamwise vortex generation mechanisms and subsequently understand the interaction of various mechanisms in a controlled manner.

This paper, then, is a report on a fundamental study on streamwise vortices generated in laminar flow through a two-dimensional nozzle that is partially blocked along the top edge of the duct exit. This is shown schematically in figure 1 and is described in detail in § 3. This blockage is referred to in the industry as a 'slice knife' or 'knife'. It was originally used to mechanically control spanwise fibre concentration by adjusting the local exit height; where there was high fibre concentration, the gap would be narrowed. Modern day headboxes use upstream dilution control, but the knife frequently remains in headbox designs as an historical artifact. Because of the extreme curvature imparted to the flow at the headbox exit, it was decided to focus first on flow past the partial blockage. The fundamental fluid dynamics questions directly associated with the blockage are: (i) does the partial blockage at the exit generate streamwise vortices? And (ii) can these vortices persist when subjected to upstream turbulence?

By virtue of the geometry, it is also possible and scientifically interesting to simultaneously examine the effect of the blockage on the turbulent boundary layer

https://doi.org/10.1017/S0022112007008300 Published online by Cambridge University Press

developing on the opposite, i.e. bottom, wall of the channel. In particular, it is an excellent opportunity to examine the effect of acceleration on turbulent boundary layer structure. The partial blockage causes intense streamwise acceleration and streamline curvature with the potential for relaminarizing the boundary layer on the opposing wall. The issue of relaminarization has as much technological importance in paper making as it does scientific importance in the field of turbulent boundary layers. The randomness and uniformity of pulp fibre orientation in the finished sheet will depend strongly on whether or not turbulence is maintained throughout the mixing region of a paper machine. Thus, the fundamental science of turbulent fluid dynamics has immediate cross-over relevance to the applied technology of paper making. At issue is whether or not a strong rapid contraction, with an acceleration parameter nominally much larger than the relaminarization limit, is sufficient to eliminate turbulence and turbulence production mechanisms. And, indeed, whether the acceleration parameter is appropriate for characterizing relaminarization in regions of rapid acceleration. This paper contains data from a detailed experiment specifically designed to address these questions. The goal of this work is to provide data and insights to advance the understanding and modelling of such flows.

2. A brief literature review

In considering a problem as seemingly simple as flow exiting a partially blocked duct, one that quickly recognizes there is that a high degree of complexity. There are no-slip boundaries, regions of high streamline curvature and a step-discontinuity in boundary conditions (i.e. no slip to shear free) as the flow exits the duct. The following literature review is structured to identify some of the hydrodynamic considerations and provide background knowledge in these areas.

2.1. *Spanwise vortices associated with flow over corners*

The dominant complexity caused by blockage at the exit of a duct is that the flow must be strongly diverted and accelerated at the exit plane. Perhaps the fundamental fluid dynamic problem most relevant to this geometry is the forward-facing-step. The flow immediately upstream of the step is characterized by a spanwise vortex that scales on the step height. Mei & Plotkin (1986) used finite-difference computational fluid dynamics (CFD) techniques to examine this flow. As their primary interest appeared to be in validating their computational methodology, they did not provide much insight into the origins and stability of the spanwise vortex. Indeed, the forward-facing step has attracted relatively little attention other than for validating computations.

2.2. *Streamwise Görtler vortex formation in boundary layer flows over concave walls*

As noted earlier, the partial blockage at the duct exit necessitates strong concave streamline curvature as fluid close to the upper wall is deflected downward by the blockage. Görtler (1940) showed that a laminar boundary layer can be unstable along a concave wall. Amplification of the instability gives rise to a system of counter-rotating streamwise vortices spanning the entire flow width. As discussed in Sherman (1990), Görtler vortices form if the Görtler number, G, is greater than 0.31. The Görtler number is defined as $G = \{U\theta/\nu\}(\theta/R)^{1/2}$, where U, θ, ν and R are the free-stream speed, boundary-layer momentum thickness, fluid kinematic viscosity and wall radius of curvature, respectively. The stability analysis does not, however, provide a way of estimating the preferred vortex size or spacing.

Rothenflue & King (1996) used laser Doppler anemometry (LDA) to measure velocities associated with Görtler vortices. Using a dimensionless wavelength

https://doi.org/10.1017/S0022112007008300 Published online by Cambridge University Press

parameter, $\Lambda = \{U\lambda/\nu\}\ (\lambda/\mathrm{R})^{1/2}$, they observed that the most unstable Görtler wavelengths occur in the range, $150 \leqslant \Lambda \leqslant 500$. Here, λ denotes Görtler wavelength.

In a series of studies, Swearingen & Blackwelder (1987) and Myose & Blackwelder (1991, 1994), examined the role of Görtler vortices in transition to turbulence over concave walls. They showed that Görtler vortices do not directly break down into turbulence. Rather, these streamwise vortices undergo a transitional stage before becoming fully turbulent.

2.3. *Streamwise vortices in free-shear layers between streams of different speeds*

Unlike the classic Görtler problem, streamline curvature upstream of the duct exit is not directly due to wall curvature. Rather, the boundary layer well upstream of the blockage separates as it approaches the exit. In this manner, the flow acquires characteristics of a free-shear layer. It is well known that a free-shear layer, formed by adjacent streams moving at different speeds, develops an inflectional profile which is unstable to Kelvin–Helmholtz type instabilities. These instabilities lead to the roll-up of spanwise vortices that scale on the shear layer thickness.

Brown & Roshko (1974) conducted a classic flow visualization study showing not only the large Kelvin–Helmholtz 'rollers', but the organized small-scale are structure as well. These small scales are manifested as a system of counter-rotating streamwise vortices entraining from one roller to the next and spanning the width of the shear layer. These streamwise vortices have been shown to be highly energetic and a critical turbulence transport mechanism in free-shear flows. For a detailed study of these streamwise vortices, see Wei & Smith (1986).

2.4. *Coherent structure in turbulent boundary layer flows*

There appears to be significant agreement in the papermaking community that coherent structures in headbox wall boundary layers may contribute to streakiness in paper. An entire field of fundamental turbulent boundary layer structure research originated from the seminal flow visualization study of Kline *et al.* (1967). They identified three key features in a turbulent boundary layer, which they named 'bursts', 'sweeps' and 'streaks' (not to be confused with paper streaks). Blackwelder & Eckelmann (1979) showed that pairs of counter-rotating vortices very close to the wall cause turbulent boundary layer streaks. Smith & Schwartz (1983) later showed that the spanwise wavelength spacing between adjacent streaks was 100 viscous lengths. For a detailed review of turbulent boundary layer structure, see Robinson (1991). Kim & Adrian (1999) used a turbulent pipe flow to study very large-scale motions (VLSM) with streamwise lengths 2–14 times the pipe radius. They defined VLSM to be a hierarchy of coherent structures. At the smallest scale were hairpin vortices, which appeared in groups. Groups of hairpin vortices were observed to form packets which, in turn, combined to form VLSM. The role of VLSM in paper streak formation was suggested by Eloranta (2000).

2.5. *The effect of favourable pressure gradients on turbulent boundary layer structure*

A common feature of headbox design is the use of a convergent nozzle, with a 5°–10° convergence angle, to maintain a continuous, moderate axial strain field on the fibre-laden flow until it exits the nozzle. From a hydrodynamic perspective, this convergence imposes a favourable pressure gradient or acceleration on the flow which may alter the turbulence interactions in the nozzle. This brings to the fore the issue of relaminarization in boundary layers.

The effects of acceleration on a turbulent boundary layer have been extensively reported in the literature. Experiments both with constant streamwise pressure

https://doi.org/10.1017/S0022112007008300 Published online by Cambridge University Press

gradient and spatially varying acceleration have been performed. In spite of the numerous studies conducted over the past four decades, a definitive parameter marking the onset of relaminarization has yet to be established. This is predominantly due to the gradual changes and somewhat overlapping boundaries between different phases in the relaminarization process.

A great deal of the past work on boundary layers under favourable pressure gradients has been concentrated on the characteristics of the mean flow. Typically published results have shown streamwise development of various time-mean quantities, such as the momentum thickness, shape factor, turbulence intensity and boundary layer thickness. Thus, these aspects are well established and the reviews by Narasimha & Sreenivasan (1979) and Sreenivasan (1982) survey these concepts and trends of relaminarization extensively. Papers by Jones & Launder (1972) and Blackwelder & Kovasznay (1971) are cornerstones in the relaminarization literature, and studies by Moretti & Kays (1965) and Badri Narayanan & Ramjee (1969) have contributed significantly.

In the light of these works, acceleration has come to be characterized by a non-dimensional acceleration parameter, K:

$$K = \left(\nu/U_\infty^2\right)\partial U_\infty/\partial x, \tag{2.1}$$

where ν is the kinematic viscosity and U_∞ is the free-stream velocity. Even though this parameter does not completely characterize the development of a boundary layer under acceleration, the value of $K > 3.0 \times 10^{-6}$ has been identified as a critical threshold value for relaminarization to occur.

There are several interesting more recent studies which were focused on turbulent coherent structures during relaminarization. Escudier *et al.* (1998) presented an experimental study using a streamline from an analytical solution of a forward-facing step flow as the upper the wall in their channel flow. Thus they eliminated the corner flow, which is of interest in the present work. Talamelli *et al.* (2002) experimentally studied acceleration in a convergent channel with the emphasis on the streaky structures in the inner part of the boundary layer. Fernholz & Warnack (1998) and Warnack & Fernholz (1998) studied axisymmetric boundary layers with different initial Reynolds numbers and acceleration distributions.

The development of computational methods during the last two decades has created important simulated data on the subject. Spalart (1986) used direct numerical simulation (DNS) to study acceleration in a sink flow. Piomelli, Balaras & Pascarelli (2000) used large-eddy simulations (LES) to explain the dynamics of flow structures in a spatially accelerating boundary layer.

The main conclusion of all these studies, experimental and computational, is that a strong enough acceleration can cause an initially turbulent boundary layer to transition into a quasi-laminar state, which resembles a laminar boundary layer. Escudier *et al.* (1998) demonstrated that in this process the intermittency factor decreases throughout the boundary layer. Spalart (1986) and Piomelli *et al.* (2000) also illustrated this phenomenon using numerical techniques. During relaminarization, streaky structures inside the boundary layer are strongly elongated in the streamwise direction. Eventually, laminar patches appear in the flow and start to grow in the downstream direction, finally taking over the entire flow field. Turbulent energy shifts to the larger scales. Fewer ejections into the outer layer are also observed. However, compared to transition to turbulence, changes associated with relaminarization occur over much longer spatial and temporal scales.

https://doi.org/10.1017/S0022112007008300 Published online by Cambridge University Press

2.6. *Summary*

This brief overview highlights a number of hydrodynamic phenomena that may be present in the partially blocked exit flow. One would certainly expect some sort of standing spanwise vortex in the corner region immediately upstream of the blockage at the duct exit. Since turbulent shear layers are frequently characterized by counter-rotating streamwise vortices, one would expect to find such vortices here as well. It is difficult to know *a priori* what the origins of these vortices are or how the blockage will affect the boundary layer on the opposing wall. This investigation was therefore structured to integrate knowledge and methodologies from fundamental hydrodynamics into a papermaking problem.

3. Experimental apparatus and methods

3.1. *The rectangular duct*

Experiments were conducted in the large free-surface water tunnel described in Smith (1992) and Grega *et al.* (1995). The facility consists of an upstream end tank with settling chamber, contraction, test section, downstream end tank, and two pumps. The test section dimensions were 610 cm (length), 122 cm (depth), and 57.2 cm (width). The walls and floor were glass, allowing maximum optical access. The maximum flow rate was 1500 l min^{-1}, corresponding to a free-stream speed of $\sim$30 cm s^{-1} when the test section is full. The free-stream velocity was found to be uniform to within $\pm$2 % across the cross-section and turbulence intensities were less than 0.1 % of the free-stream speed.

A schematic drawing of the rectangular duct with partial blockage is shown in figure 1. The upper wall of the duct was an acrylic plate, 57.2 cm wide, 70 cm long and 1.27 cm thick. It was smoothly connected to the contraction exit by a stiff, but flexible, connection. The angle of the top wall could be adjusted to consider duct convergence effects. Only horizontal upper-wall data are presented in this paper. A convergent nozzle case was presented in Hsu & Wei (2004). The sidewalls and floor of the water tunnel test section were also the sides and floor of the duct.

The partial blockage at the duct exit was a 57.2 cm wide, 20 cm high piece of 1.27 cm thick acrylic attached to the downstream edge of the upper duct wall. The blockage was oriented perpendicular to the upper wall regardless of convergence angle. For the present study, the blockage height was 5.08 cm with a corresponding duct exit opening of 5.08 cm. Note that for this opening, the top of the blockage extends above the top wall of the duct. A piece of aluminum angle mounted to the top wall was used to hold the blockage in place. This is not shown in figure 1.

A false floor/bottom wall was made of 57.2 cm wide sheets of 0.64 cm thick plastic bolted to two 610 cm long steel rails. The leading edge of the floor was aligned with the test section inlet and extended more than 25 cm downstream of the rectangular channel exit. The top surface of the bottom wall was $\sim$4 cm above the water-tunnel test section floor. Seams between adjacent floor panels were taped so that the maximum roughness along the bottom wall was less than 0.005 cm. For the turbulent boundary layer relaminarization studies, a rectangular bump was placed across the bottom wall at the test section inlet to serve as a turbulent boundary layer trip.

To ensure that uniform laminar flow entered the duct (apart from the boundary layer trip for the relaminarization component of this work), a two-dimensional contraction was constructed. The contraction curve was defined using Morel's (1977) work on two-dimensional wind-tunnel inlet design. A 10:1 contraction was used with an exit height

https://doi.org/10.1017/S0022112007008300 Published online by Cambridge University Press

of 10.16 cm and overall length of 152.4 cm. The curvature consisted of matched cubic splines with the matching point at the mid-length. The contraction was constructed using thin sheets of PVC welded and glued to a PVC framework of ribs and spars. The ribs were pre-cut to the exact shape and dimensions of the desired contraction curve. Note that, for the experiments described in this paper, the water level upstream of the contraction was not up to the top of the contraction. This is indicated in figure 1.

To accommodate LIF flow visualization studies, a dye injection slot, 0.16 cm wide $\times$ 10 cm long, was machined into the top wall of the duct. The slot was aligned in the cross-stream direction and centred on the mid-span of the plate. It was 15.24 cm upstream of the duct exit plane.

The entire duct assembly, including the two-dimensional contraction, could be placed at any point along the water tunnel. For the top-wall near-corner studies, the duct assembly was placed as far upstream in the test section as possible. In this phase of the investigation, the entrance to the contraction was $\sim$10 cm downstream of the test section inlet. For the relaminarization experiments, the duct assembly was installed in the test section with the contraction entrance $\sim$150 cm downstream of the test section inlet. In this case, the duct entrance was then $\sim$300 cm from the test section inlet and the partially blocked exit was $\sim$370 cm from the inlet.

3.2. *The DPIV measurement system*

Data presented in this paper were acquired over two separate time periods using the same facility and equipment, but different software. For the component of the research addressing stability and origins of vortices formed by the exit blockage, a high-resolution digital particle image velocimetry (DPIV) system, developed in-house, was used to obtain velocity and vorticity data. A commercial DPIV system was used to process images acquired for the relaminarization part of the work. A description of the DPIV technique is provided in Willert & Gharib (1991). Details of the in-house system may be found in Hsu (2000).

Flow was seeded using 13 μm silver-coated hollow glass spheres with specific gravity of 1.6 and illuminated using a dual head Nd:YAG laser (New Wave Gemini PIV 120-15) capable of producing two laser pulses at 1/15 s intervals with output energies of 120 mJ per pulse. The time between pulses could be set as small as 0.5 μs. The time interval between successive images in a DPIV image pair was 100 μs $\leqslant \Delta t \leqslant$ 500 μs. Shorter Δt values were used for end-view (y, z plane) measurements while larger Δt were used for plan-view and side-view measurements. Timing was controlled using a Stanford Research Systems DG535 digital delay/pulse generator operating at 15 Hz. A Kodak Megaplus ES 1.0 digital video camera with 1008 $\times$ 1018 pixel resolution was used to capture video records of seeded flow. The camera output was connected to an Imaging Technology IC-PCI image-capture board located on a 300 MHz Pentium PC. This permitted capture of 450 consecutive video frames, i.e. 225 DPIV vector fields, corresponding to $\sim$15 s long records of the flow. For every measurement location, five sets of 225 vector fields were captured. The total sampling time for each data set exceeded 25 minutes.

The in-house DPIV image processing software is reported in Hsu *et al.* (2000). The program employed a two-stage correlation algorithm in which a large, 128 $\times$ 128 pixel, interrogation window was used for a highly accurate, though spatially averaged, coarse displacement field. This was followed by a refined correlation stage in which corresponding interrogation windows were displaced by an amount prescribed by the coarse displacement field. The fine correlation windows for this study were

https://doi.org/10.1017/S0022112007008300 Published online by Cambridge University Press

Quantity	Uncertainty ($\Delta t = 500\,\mu s$)	Uncertainty ($\Delta t = 100\,\mu s$)
mean velocity, U_I	$0.015\,cm\ s^{-1}$	$0.125\,cm\ s^{-1}$
r.m.s. velocity, u_i	$0.13\,cm\ s^{-1}$	$0.54\,cm\ s^{-1}$
Reynolds stress, $\langle u_I u_j \rangle$	$0.0006\,cm^{-2}\ s^{-2}$	$0.0024\,cm^{-2}\ s^{-2}$
vorticity, $\partial U_I/\partial x_j - \partial U_j/\partial x_i$	$0.02\,s^{-1}$	$0.10\,s^{-1}$

TABLE 1. DPIV measurement uncertainties for the partially blocked channel experiment.

64×64 pixels with four times over-sampling. Spacing between adjacent velocity vectors was 0.06 cm.

Measurement uncertainties associated with the in-house DPIV software (used for the blockage vortex work) were computed from a controlled experiment described in Hsu *et al.* (2002). In brief, over 1000 DPIV vector fields were captured in the laminar potential core of the water tunnel. Based on the very conservative assumption that all spatial and temporal variations in measured velocities were due to DPIV uncertainty, uncertainties in velocity and velocity gradient quantities were computed directly from the data set. Using current fields of view and times between laser pulses, the results from Hsu *et al.* (2002) were converted for these experiments. These are summarized in table 1.

Data for the turbulent boundary layer relaminarization component of this research (i.e. the bottom wall) were computed using LaVision's software package, DaVis. Use of DaVis required development of an in-house vector validation algorithm to detect and replace spurious vectors. Validation criteria included ensuring each vector magnitude was within a range of acceptable velocities and local median filtering. Based on these criteria, less than 1 % of all vectors were determined to be spurious. Each bad vector was replaced by the mean of its eight neighbours.

3.3. *Experimental conditions for the near-corner flow studies*

All data sets associated with understanding the near-corner flow approaching the blockage on the upper wall were taken ~70 cm downstream of the duct inlet; this was ~270 cm downstream of the test section inlet. The water level on the upstream side of the duct was fixed at 44.5 cm. The upstream speed in the test section was $20\,cm\,s^{-1}$. DPIV measurements were made in orthogonal planes at various positions upstream of the duct exit. Measurements were not made downstream of the duct.

3.4. *Experimental conditions for the relaminarization studies*

For the relaminarization experiments, the velocity upstream of the contraction was $15\,cm\,s^{-1}$. Flow accelerated through the contraction to $100\ cm\,s^{-1}$ in the rectangular channel section. DPIV measurements were made principally in the x, y plane. For each measurement location one thousand instantaneous velocity fields were captured at a sampling rate of 15 Hz. DPIV interrogation windows were 32×32 pixels with 50 % overlap. The camera field of view for these measurements was $2.54\,cm \times 2.54\,cm$. Data presented in this paper are focused on the region approaching the partially blocked rectangular channel exit. For the complete data set, including measurements in three orthogonal planes, spanning the entire variable height duct, the reader is referred to Eloranta (2005).

https://doi.org/10.1017/S0022112007008300 Published online by Cambridge University Press

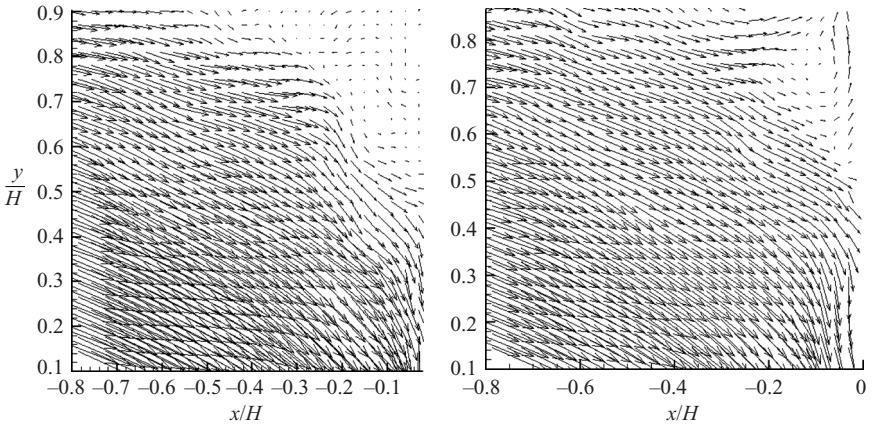


FIGURE 2. Two instantaneous DPIV vector fields showing flow in the near-corner region. Flow is left to right with the channel exit located at $x/H = 0$.

4. Results and discussion; the near-corner region along the top wall

End-view (y, z), plan-view (x, z) and side-view (x, y) measurements were made at various locations immediately upstream of the partial blockage. Careful analysis of the DPIV vector fields produced a picture of turbulence generated in the corner formed by the duct top wall and partial blockage emerged. This included formation of an unsteady spanwise vortex in the near-corner region and turbulent streamwise vortices emanating from that spanwise vortex. Vortices generated at the partially blocked exit appeared to be quite robust even in the presence of upstream turbulence.

The coordinate system for data presented throughout this section has x and z as the streamwise and spanwise directions, respectively. The y-direction is aligned with gravity, i.e. down, normal to the bottom wall of the duct. The origin is centred at the mid-span of the test section, and located at the bottom, leading edge of the blockage. All measurements were made upstream of the blockage corresponding to $x < 0$. Vertical positions between the top wall and bottom of the blockage bar correspond to $y > 0$; negative y-coordinates are located below the bar. Data for the near-corner studies have been non-dimensionalized by the freestream velocity in the test section, upstream of the duct, $U_0 = 20\,\mathrm{cm\,s^{-1}}$, and blockage height, $H = 5.08\,\mathrm{cm}$.

4.1. *Spanwise vortex in the corner formed by the duct top wall and vertical blockage bar*

It is important to note at the outset that flow through the duct without the partial blockage was laminar. This is shown in Hsu (2002) where a Blasius boundary layer profile was fitted to the boundary layer measured on the top wall of the duct. In addition, turbulence intensities were found to be less than 1 % of the local free-stream velocity when the blockage was not present.

When the blockage was in place, however, the flow became dramatically different. Two instantaneous side-view DPIV vector fields showing flow in the corner bounded by the horizontal top-wall and the 5.08 cm horizontal blockage appear in figure 2. Flow is left to right with the upstream face of the blockage bar located at $x/H = 0$. The bottom edge of the blockage corresponds to $y/H = 0$. The existence of strong spanwise vortices is clearly evident in both vector fields. Animated sequences of successive DPIV fields show a highly dynamic flow in which one or more vortices move about in the corner region.

https://doi.org/10.1017/S0022112007008300 Published online by Cambridge University Press

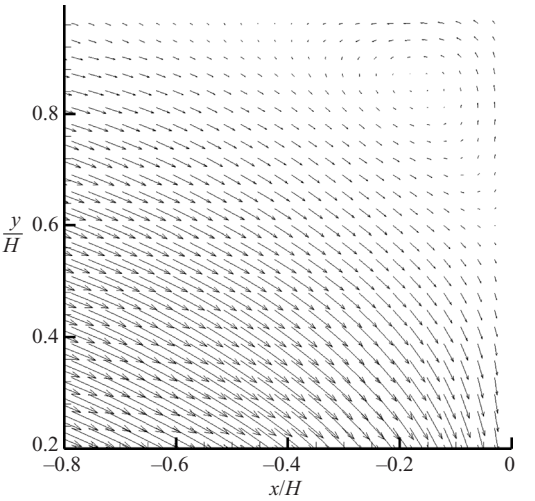


FIGURE 3. Ensemble average of 1000 instantaneous DPIV vector fields (see figure 2). Observe the mean corner vortex centred at $(x, y) = (-0.15, 0.85)$.

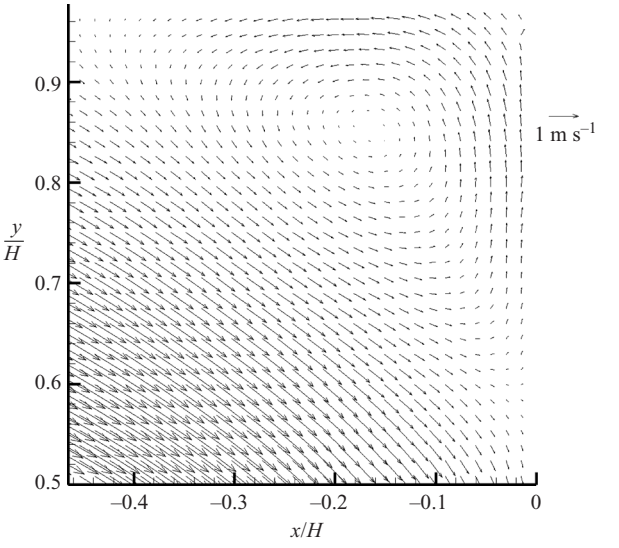


FIGURE 4. Close-up of the time-averaged velocity field in the near-corner region. See figure 3.

A time-averaged vector field showing the mean corner vortex appears in figure 3. This field was computed by ensemble averaging over 1000 instantaneous fields acquired at 15 fields per second. A close up of the near-corner region is shown in figure 4. Observe that the corner vortex occupies a significant portion of the corner region. Both its streamwise and vertical dimensions are approximately 40 % of the blockage height. Contour plots showing turbulence intensities in the streamwise and wall-normal directions are shown in figure 5. Plan-view contours of spanwise turbulence intensities are shown in figure 6. Measurements in figure 6 were made in a plane 1.27 cm above the bottom of the blockage bar.

https://doi.org/10.1017/S0022112007008300 Published online by Cambridge University Press

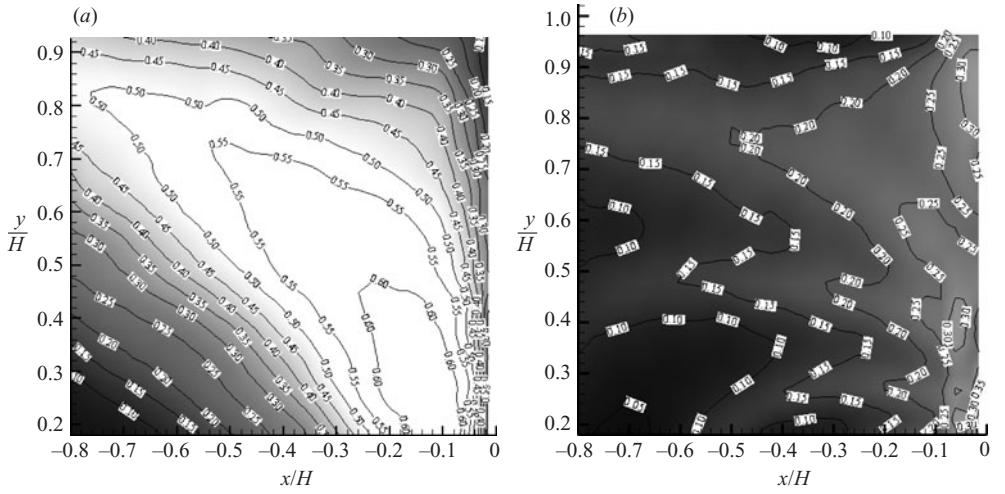


FIGURE 5. Streamwise (*a*) and vertical (*b*) turbulence intensity in the corner region upstream of the partial blockage.

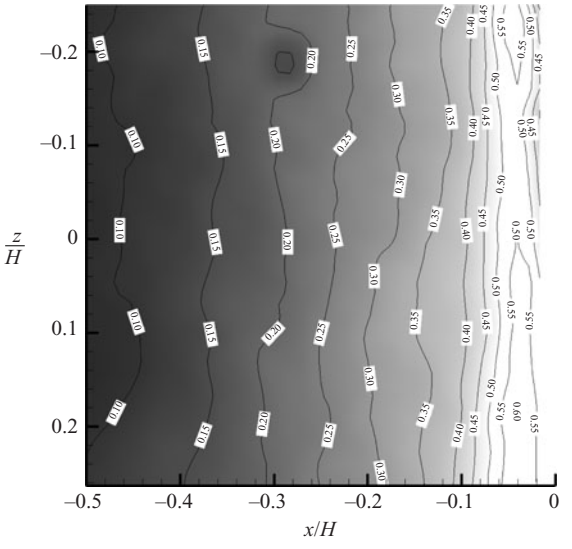


FIGURE 6. Distribution of spanwise turbulence intensity, w'/U_o, measured in a plane at the mid-height of the blockage bar, $y/H = 0.5$.

4.2. *Streamwise vortex generated at the partially blocked duct exit*

Figures 2–6 clearly confirm the motivating premise of this investigation, i.e. that the 'knife' plays a critical role in paper machine hydrodynamics. The formation of an unsteady spanwise vortex and the abrupt change in boundary conditions at the partially blocked exit (no slip to shear free) are significant. Perhaps of greater interest from both fluid dynamics as well as papermaking perspectives, however, is the high degree of three-dimensionality arising from this corner vortex. Specifically, evidence of strong streamwise vortices could be found in horizontal, plan-view DPIV measurement planes. This is shown in figures 7 and 8. Figure 7 is an instantaneous LIF flow visualization image showing flow in the plane of the exit, the y, z plane.

https://doi.org/10.1017/S0022112007008300 Published online by Cambridge University Press

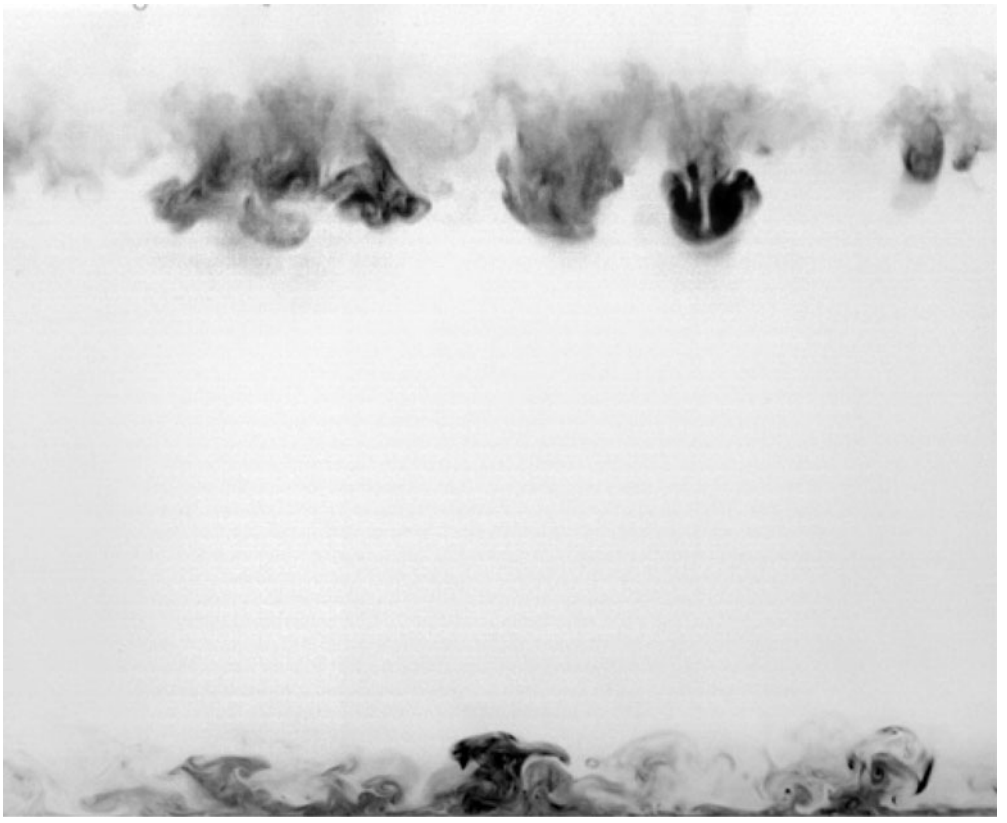


FIGURE 7. Instantaneous end-view, y, z-plane, LIF flow visualization image showing counter-rotating vortices streaming under the partially blocked exit. Flow is out of the page. The bottom edge of the blockage appears across the top of the image and the duct bottom wall appears across the bottom. The grey-scale has been inverted so that the fluorescing dye appears as black in the picture.

Flow is out of the page and the bottom edge of the blockage appears across the top of the image. Note that the grey-scale has been inverted so that the fluorescing dye appears as black in the picture. The presence of counter-rotating vortices streaming out immediately under the blockage are clearly evident in this image.

Figure 8 contains an instantaneous DPIV vector field captured just upstream of the bottom, leading edge of the blockage, i.e. at $y/H = 0$. Flow is left to right with $x/H = 0$ denoting the blockage location. The remarkable feature in figure 8 is the presence of strong counter-rotating vortices. Looking back at figure 3, it can be seen that flow immediately upstream of the blockage is virtually straight down as fluid is forced to turn down, out of the way of the obstruction. At, and immediately downstream of the partially blocked duct exit, the flow abruptly turns back into the main flow direction as the jet exits the duct. Upstream of the blockage, for $y/H \geqslant 0$, then, horizontal x, z planes show the same counter-rotating vortices seen in the cross-stream LIF image in figure 7. Thus, vortices appearing in figure 8 should be interpreted as streamwise vortices that are realigned in the wall-normal direction as they pass under the blockage.

The robustness of the streamwise vortex generation mechanism was examined. This was done by placing stainless-steel screens upstream of the duct. Two different

https://doi.org/10.1017/S0022112007008300 Published online by Cambridge University Press

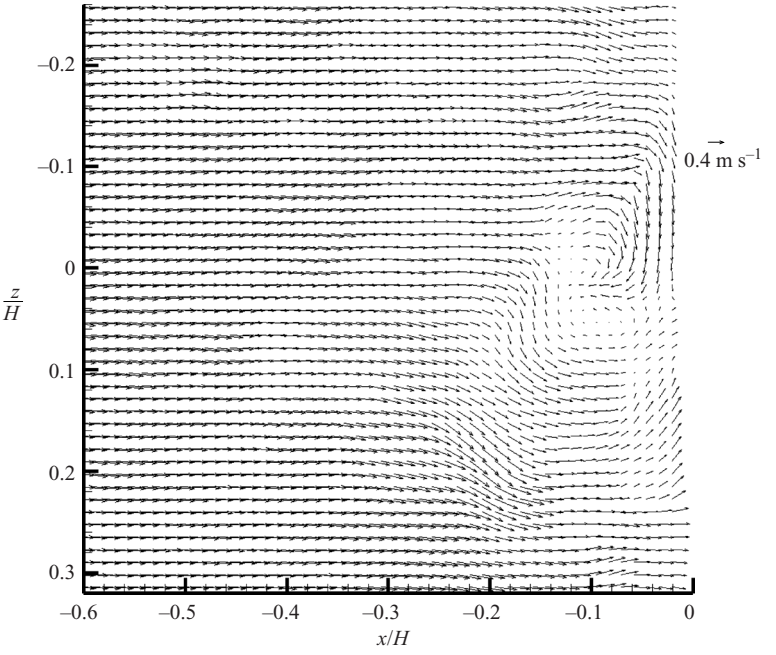


FIGURE 8. Instantaneous plan-view DPIV vector field showing streamwise vortices. These vortices are made visible in the x, z-plane because the flow turns down as it approaches the partially blocked channel exit.

mesh and wire sizes were used as turbulent generators. In both cases, the streamwise vortices were the dominant feature of the exit flow. This is also discussed in Hsu & Wei (2004).

5. Results and discussion; pressure gradient effects on the bottom-wall turbulent boundary layer

Before presenting data from the bottom-wall turbulent boundary layer, it is essential to note the change in coordinate system. The origin of the coordinate system up to now has been located on the bottom wall of the duct directly below the *trailing* edge of the blockage. The y-direction now points *up* away from the bottom wall. The x-direction still points upstream but positive streamwise velocities correspond to the downstream direction.

Because of spatial resolution limitations in the rectangular channel and under the blockage, the friction velocity u_τ could not be accurately determined. Thus, turbulence quantities obtained in this study could not be plotted in wall variables and another approach to non-dimensionalization had to be adopted. Following the approach of Blackwelder & Kovasznay (1972) and Escudier *et al.* (1998), the wall-normal distance can be expressed in terms of the stream function, $\psi(x, y)$ non-dimensionalized by kinematic viscosity, ν. Since DPIV measurements in the x, y-plane extend to the bottom wall, the velocity data can be integrated in the wall-normal direction to yield:

$$\frac{\psi}{\nu} = \frac{1}{\nu}\int_0^y U(y)\,\mathrm{d}y,$$

https://doi.org/10.1017/S0022112007008300 Published online by Cambridge University Press

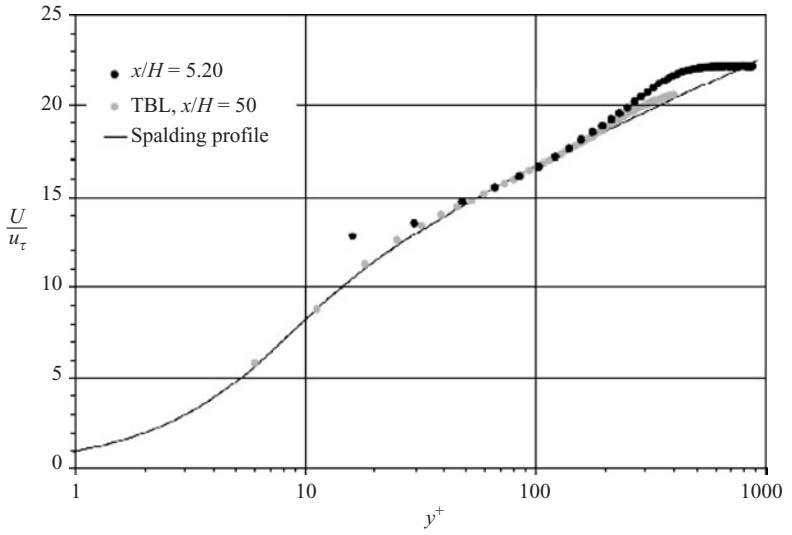


FIGURE 9. Mean streamwise velocity profiles measured upstream, $x/H = 50$, and downstream, $x/H = 5.2$, of the laminar two-dimensional contraction. Data are scaled on inner variables.

where U is the mean streamwise velocity and y distance from the wall. This is a convenient way to express the wall-normal coordinate when the streamlines are not parallel to the wall. Throughout this paper, profiles of turbulence intensities and Reynolds stresses are also presented using stream coordinates rather than actual distances from the wall.

Owing to the complexity of the variable height duct, it was important to validate the DPIV measurement technique and establish some reference baseline. In addition, it would be helpful at this point to develop a sense of the degree of distortion imposed on the bottom-wall turbulent boundary layer by the variable height duct. To these ends, velocity measurements are presented in figures 9 and 10, both upstream of the two-dimensional contraction and in the rectangular channel section, that is, 250 cm ($x/H = 50$) and 26 cm ($x/H = 5.2$) upstream of the partially blocked exit, respectively. The former data were taken upstream of the headbox model and demonstrate the existence of a canonical turbulent boundary layer as the inlet conditions to the rest of the flow.

Mean streamwise velocity profiles at these two stations are presented in figure 9. Data are non-dimensionalized using friction velocity values found by fitting mean velocity data to the Spalding profile. Corresponding profiles for u'/u_τ and v'/u_τ are shown in figure 10. The first point to note is that upstream of the two-dimensional contraction, there is a canonical turbulent boundary layer. The second feature is that there are differences between the upstream canonical boundary layer and the boundary layer in the rectangular channel section. Observe that the streamwise turbulence intensity values in the rectangular channel are slightly lower than those in the reference boundary layer. There is also a secondary peak in the u'/u_τ profile at $y^+ = 150$. The significance or origin of this secondary peak cannot be evaluated from the present data. The agreement between the wall-normal turbulence intensity profiles is better. Some properties of the boundary layer at this position are listed in table 2.

5.1. *Characteristics of the acceleration zone*

The streamwise variation of local mean free-stream velocity, $U_\infty(x)$, for $5.2 \geqslant x/H \geqslant 0$, is shown in figure 11. Velocity values are non-dimensionalized by U_o, the free-stream

https://doi.org/10.1017/S0022112007008300 Published online by Cambridge University Press

$\delta\ (U/U_o = 0.995)$	$0.21H$ (1.05 cm)
δ^*	$0.028H$ (0.142 cm)
θ	$0.216H$ (0.108 cm)
Re_θ	1100

TABLE 2. Key turbulent boundary layer parameter values at $x/H = 5.2$.

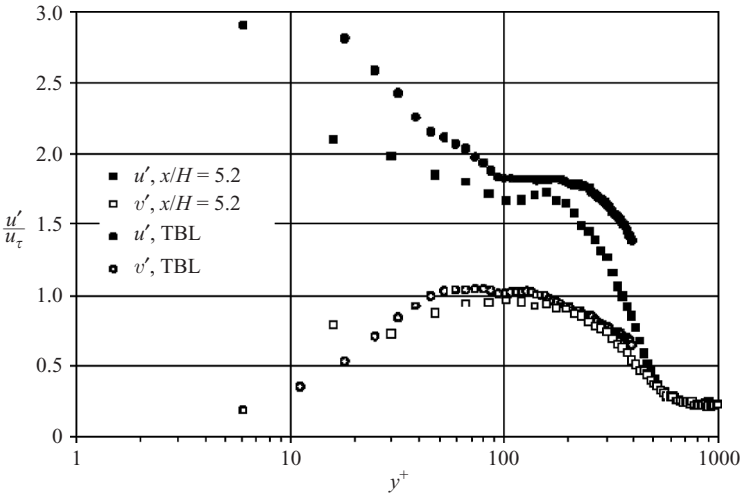


FIGURE 10. Streamwise and wall-normal turbulence intensity profiles measured both upstream and downstream of the laminar contraction. □, u'/u_τ at $x/H = 50$; ■, u'/u_τ at $x/H = 5.2$; ○, v'/u_τ at $x/H = 50$; ●, v'/u_τ at $x/H = 5.2$.

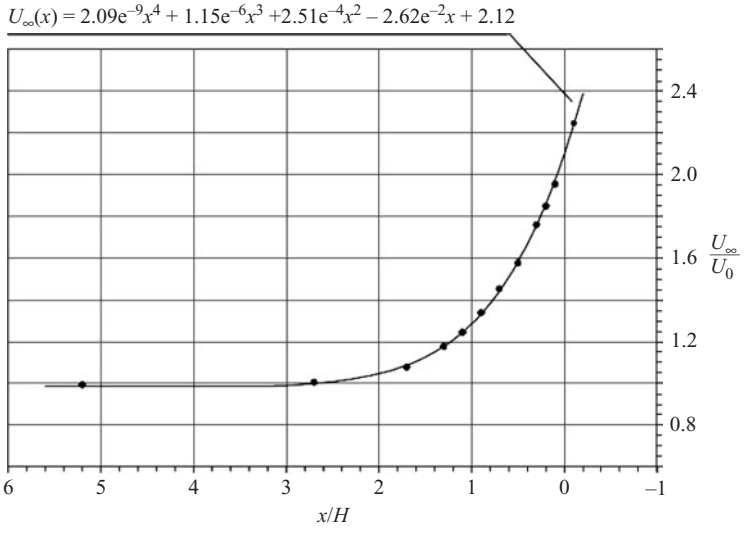


FIGURE 11. Variation in free-stream velocity with streamwise position along the channel.

https://doi.org/10.1017/S0022112007008300 Published online by Cambridge University Press

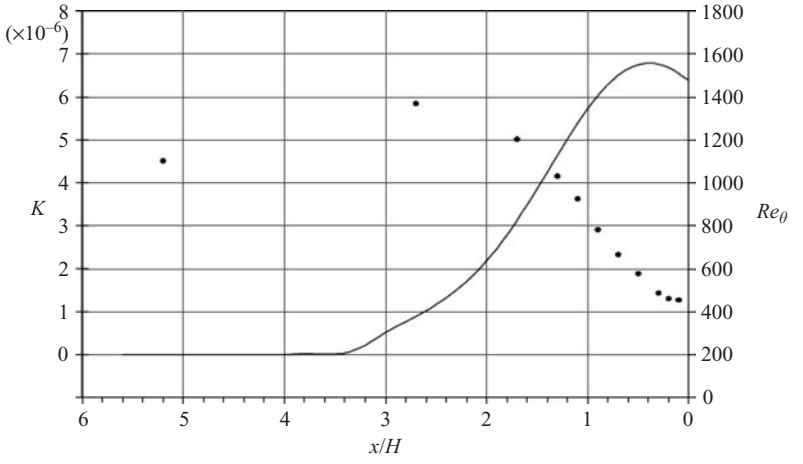


FIGURE 12. Variations of acceleration parameter, K, (solid line) and momentum-thickness Reynolds number, Re_θ, ● as functions of non-dimensional streamwise position, x/H.

speed at $x/h = 5.2$; recall that this is 1.0 m s^{-1}. A fourth-order polynomial fit to the measured velocity values is included in the plot. In the following, this polynomial has been differentiated to obtain a smooth estimate for the streamwise velocity gradient needed for the computation of the acceleration parameter K. The influence of the partial blockage begins at $x \approx 2.7H$. This is indicated by slightly elevated free-stream velocity. Just under the blockage, the local free-stream velocity, $U_\infty(x)$, is 2.1 times faster than U_o.

Streamwise evolution of the acceleration parameter $K(x)$ is presented in figure 12. Observe that K increases from zero for $x/H \geqslant 3.4$ to a maximum of 6.75×10^{-6} at $x/H \approx 0.4$. Downstream of this peak, the acceleration parameter decreases, at least to the partial blockage. In addition, note that K crosses the threshold value of 3.0×10^{-6} around $x/H \approx 1.7$. This is the threshold value that is widely accepted as the relaminarization limit; for $K > 3.0 \times 10^{-6}$, turbulence should rapidly decay and the boundary layer should become laminar.

Figure 12 also shows the development of the Reynolds number based on the boundary layer momentum thickness, Re_θ. The boundary layer thickness increases between $x/H = 5.2$ and $x/H = 2.7$. Re_θ appears to reach a maximum around $x/H \approx 2.7$ and subsequently decreases almost linearly from $x/H = 1.7$ to $x/H = 0.4$. As flow begins to pass under the leading edge of the partial blockage, Re_θ appears to reach a minimum. Note that, in spite of the fact that the acceleration parameter is more than twice the nominal relaminarization threshold limit of 3.0×10^{-6}, Re_θ does not decrease below a value of 450. This is still above the limiting value of 330, found by Spalart (1986), necessary to sustain a turbulent boundary layer. The response of the turbulent boundary layer statistics to the partially blocked exit are presented in the following section.

5.2. *Variation of turbulence statistics approaching the channel exit*

Mean streamwise velocity profiles at different stations, x/H, are presented in figure 13. Two different wall parameters are used, y/H and the stream function, ψ/ν. These are plotted in figures 13(a) and 13(b), respectively. In both plots, the local mean velocities, $U(x, y)$, are non-dimensionalized by the local maximum, $U_\infty(x)$. The advantage of using streamfunction as the wall coordinate is that it is possible to compare relative

https://doi.org/10.1017/S0022112007008300 Published online by Cambridge University Press

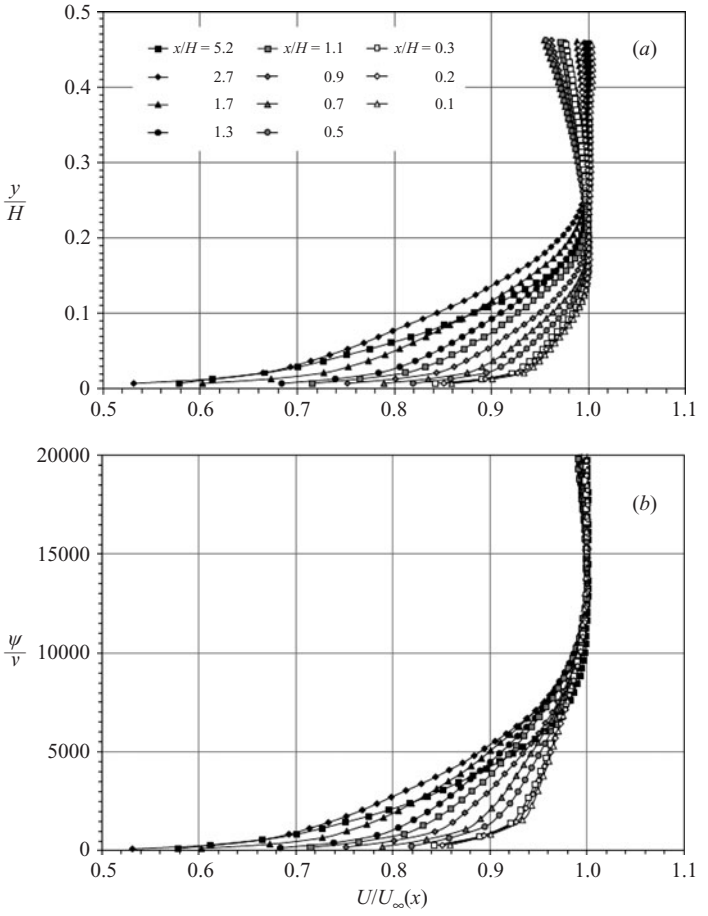


FIGURE 13. Profiles of mean streamwise velocity, normalized by local free-stream velocity, $U_\infty(x)$. Data are plotted as functions of (*a*) distance from the wall, y/H, and (*b*) streamfunction, ψ/ν. For various x/H values.

locations in the boundary layer as it is compressed under the influence of the partially blocked exit. For all of the different streamwise measurement stations, the outer edge of the boundary layer appears to be at $\psi/\nu \approx 14000$. Thus, while figure 13(*a*) shows the actual decrease in boundary layer thickness approaching the channel exit, figure 13(*b*), highlights changes in profile shape. Observe that, in the three profiles closest to the exit, $0.3 \geqslant x/H \geqslant 0.1$, a distinct kink appears in the near-wall region, $\psi/\nu \approx 1500$. In addition, those three profiles appear to be virtually linear in the range $2000 < \psi/\nu > 10000$.

Turbulence intensity profiles plotted versus streamfunction are shown in figure 14. Streamwise and wall-normal intensities appear in figures 14(*a*) and 14(*b*), respectively. The local maximum free-stream velocity, U_∞, is again used as the velocity scaling parameter. As was observed from the mean-velocity profiles, the edge of the boundary layer collapses onto a fixed streamfunction value of $\psi/\nu \approx 14000$.

One can clearly see the decrease in turbulence intensities, for both u' and v', as the flow approaches the channel exit. The damping of streamwise fluctuations is more pronounced relative to wall-normal fluctuations. Indeed for $x/H \leqslant 0.7$, except very close to the wall ($\psi/\nu < 1000$), u' becomes smaller than v'. This point will be revisited

https://doi.org/10.1017/S0022112007008300 Published online by Cambridge University Press

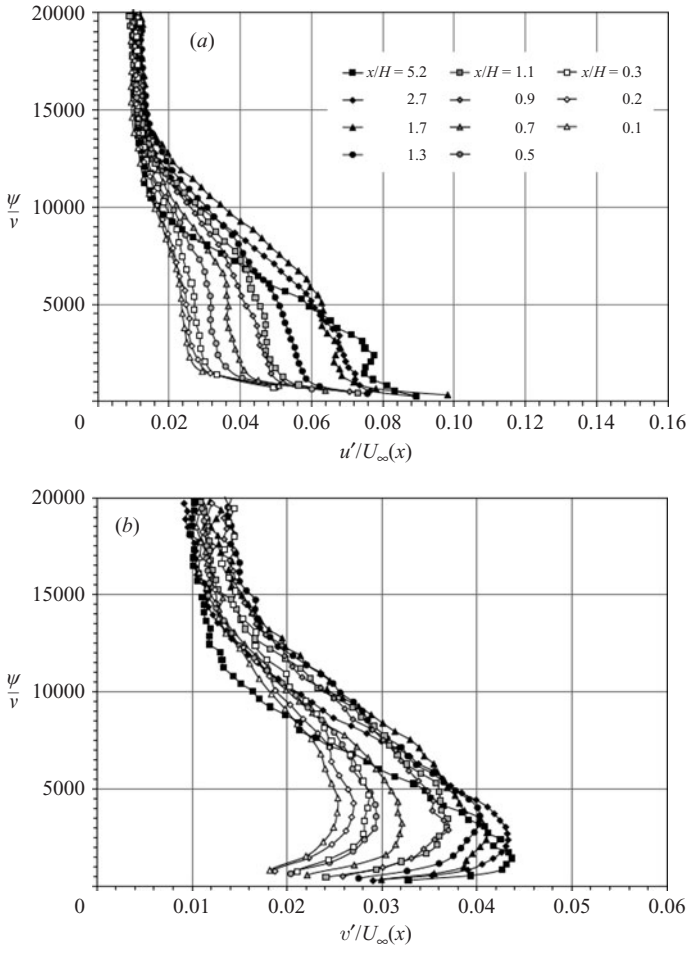


FIGURE 14. Turbulence intensity profiles (*a*) u'/U_∞ and (*b*) v'/U_∞ plotted against streamfunction, ψ/ν, for eleven different streamwise locations along the rectangular duct section.

more clearly in the presentation of figure 17. In addition, use of the streamfunction as the wall-normal coordinate also shows that the relative position of the v' peak shifts away from the wall as flow accelerates approaching the exit. Keep in mind, however, that the boundary layer thickness decreases in an absolute sense.

Figures 15 and 16 show plots of turbulence intensities, u' and v', as functions of x/H for three key streamlines, $\psi/\nu = 1000$, 3000 and 15000. These correspond to the near-wall region, the middle of the boundary layer (i.e. the log region if this were a canonical turbulent boundary layer) and the outer edge of the boundary layer, respectively. Data in figure 15 are non-dimensionalized by the local maximum velocity, $U_\infty(x)$. This provides a relative comparison between different streamwise locations. In figure 16, turbulence intensity data are scale using U_o, the free-stream velocity at $x/H = 5.2$. This provides an absolute comparison of spatial variations because U_o is a constant.

In figure 15, one can see that both u' and v' remain essentially constant outside the boundary layer, but decrease significantly within the boundary layer. This is

https://doi.org/10.1017/S0022112007008300 Published online by Cambridge University Press

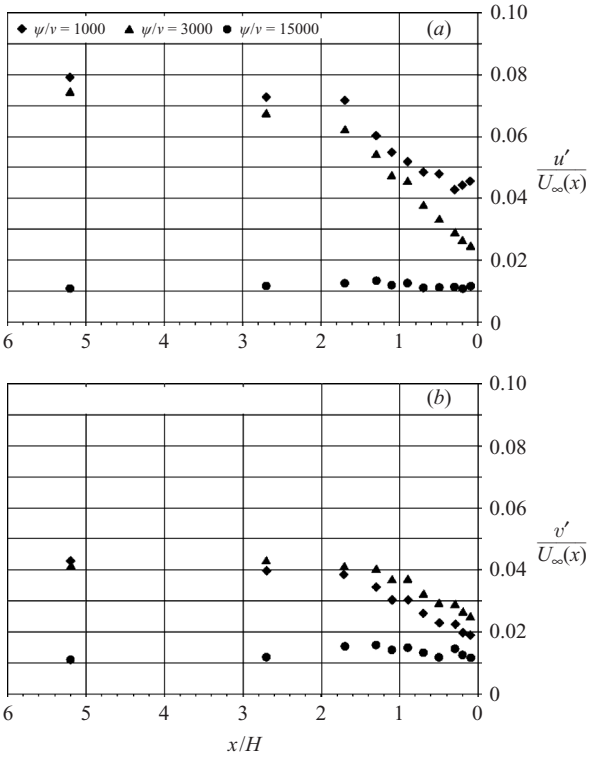


FIGURE 15. Streamwise development of (*a*) u' and (*b*) v' along three selected streamlines, $\psi/\nu = 1000$, 3000 and 15000. Data are normalized by the local free-stream velocity.

particularly true for u'. In an absolute sense, however, the picture is decidedly different. This is shown in figure 16. In this case, the intensity levels on the edge of the boundary layer increase slightly and in the near-wall area the increase is even more pronounced. Turbulence in the mid-layer, however, still decreases approaching the partially blocked exit. The key point here is that the turbulence does not disappear in spite of the fact that the acceleration parameter, K, is significantly larger than the nominal relaminarization threshold.

An observation was put forward in the presentation of figure 14 that u'decreases more than v'. This is further highlighted in figure 17 where the ratio u'/v' is plotted as a function of streamwise location, x/H, for the same three streamlines, $\psi/\nu = 1000$, 3000 and 15000. At the edge of the boundary layer, corresponding to the $\psi/\nu = 15000$ streamline, u'/v' is equal to unity upstream of $x/H \approx 2$. This may be interpreted as an indication that the boundary layer turbulence in the outer region is isotropic well upstream of the partially blocked exit.

This is naturally not the case in the mid-boundary layer, $\psi/\nu = 3000$, the region that would correspond to the log region in a canonical turbulent boundary layer. In the strong acceleration approaching the channel exit, u'/v' decreases from $\sim$1.8 at $x/H = 5.2$ to unity immediately upstream of the blockage.

Close to the wall, $\psi/\nu = 1000$, u'/v' increases from $\sim$1.8 at $x/H = 5.2$ to $\sim$2.4 at the channel exit plane at $x/H = 0$. Note from figure 16, that v' *increases* as the flow approaches the channel exit. The marked increase in u'/v', however, is due to the strong amplification in streamwise fluctuations. These results, summarized in figure 17

https://doi.org/10.1017/S0022112007008300 Published online by Cambridge University Press

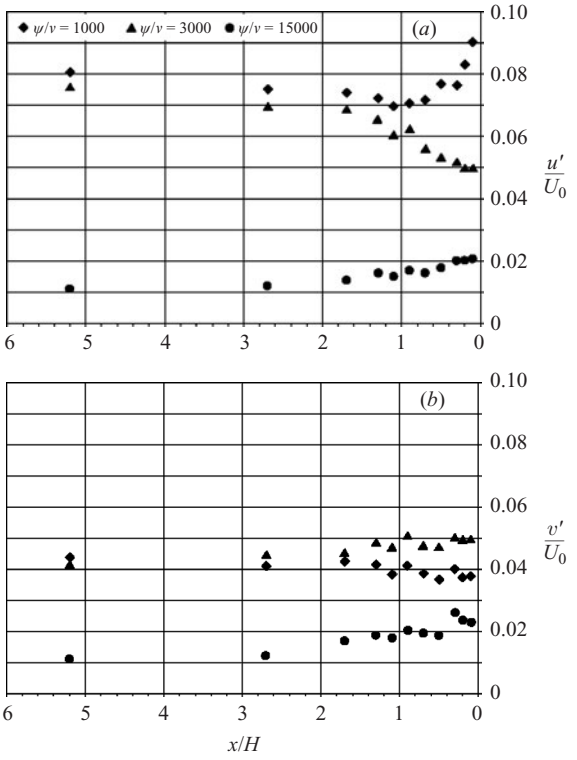


FIGURE 16. Streamwise development of (*a*) u' and (*b*) v' along three selected streamlines, $\psi/\nu = 1000$, 3000 and 15000. Data are normalized by the free-stream velocity at $x/H = 5.2$.

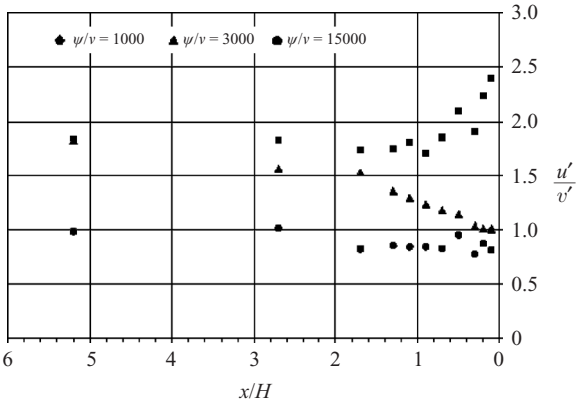


FIGURE 17. Streamwise development of u'/v' along three selected streamlines, $\psi/\nu = 1000$, 3000 and 15000. Data are normalized by the free-stream velocity at $x/H = 5.2$.

clearly indicate that the boundary layer is not relaminarizing as it approaches and passes under the partial blockage.

Reynolds stress data, $-\langle uv\rangle/U_\infty^2$, plotted versus y/H and ψ/ν at the eleven streamwise locations $5.2 \geqslant x/H \geqslant 0.1$ are shown in figures 18 and 19 respectively. Observe that the maximum Reynolds stress decreases by ~90%. Figure 19 further

https://doi.org/10.1017/S0022112007008300 Published online by Cambridge University Press

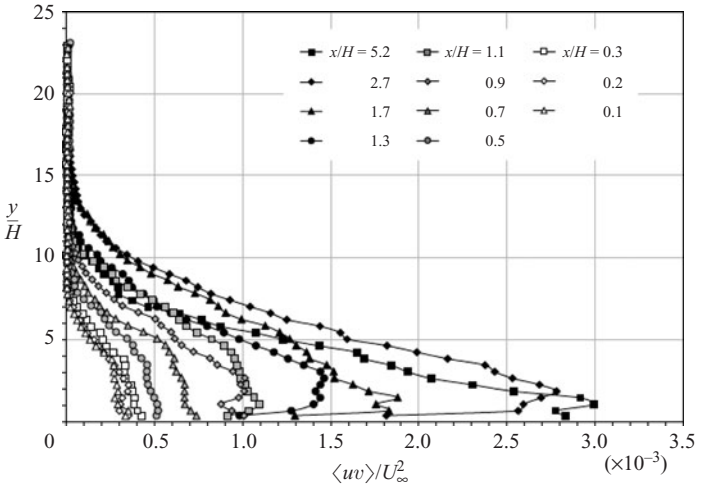


FIGURE 18. Reynolds stress profiles, non-dimensionalized by the local free-stream velocity, plotted as a function of distance from the wall, y/H.

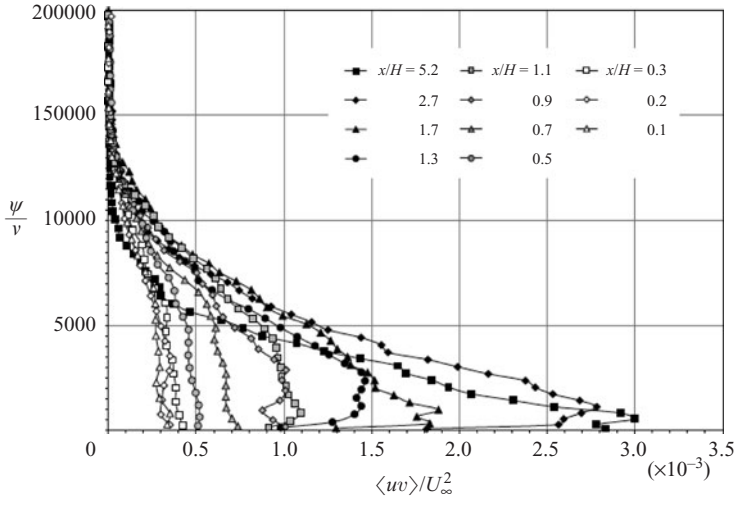


FIGURE 19. Reynolds stress *vs.* streamfunction for different streamwise locations along the channel. Data are normalized by the free-stream velocity at $x/H = 5.2$.

shows that the Reynolds stress peak broadens as a function of stream function as flow approaches the channel exit.

Streamwise variation of Reynolds stress, non-dimensionalized by U_o^2, for the three streamlines, $\psi/\nu = 1000$, 3000 and 15000, appear in figure 20. In absolute terms, the decrease in Reynolds stress approaching the channel exit is still evident, albeit not as dramatically as in figures 18 and 19. This is, of course, because the local free-stream velocity, U_∞, increase as flow passes under the partial exit blockage, whereas U_o, is a constant.

For the two inner streamlines, the decrease in $-\langle u'v'\rangle/U_o^2$ is $\sim$30 %. Farther from the wall at the edge of the boundary layer, along the $\psi/\nu = 15000$ streamline, Reynolds stress is effectively zero along the entire length of the channel as would be

https://doi.org/10.1017/S0022112007008300 Published online by Cambridge University Press

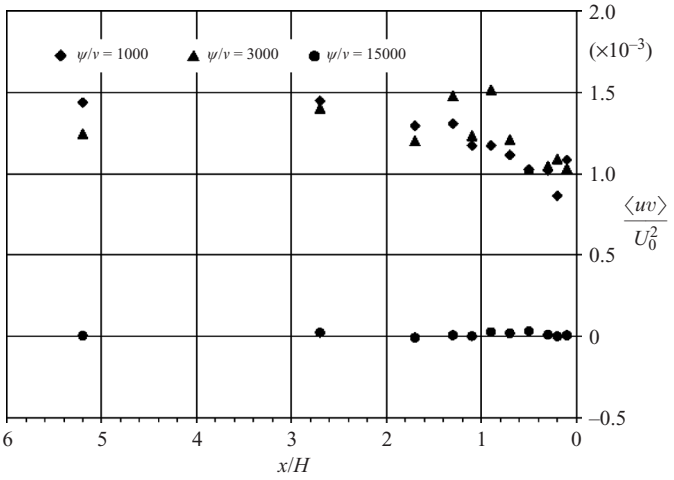


FIGURE 20. Streamwise development of Reynolds stress along three selected streamlines, $\psi/\nu = 1000$, 3000 and 15000. Data are normalized by the free-stream velocity at $x/H = 5.2$.

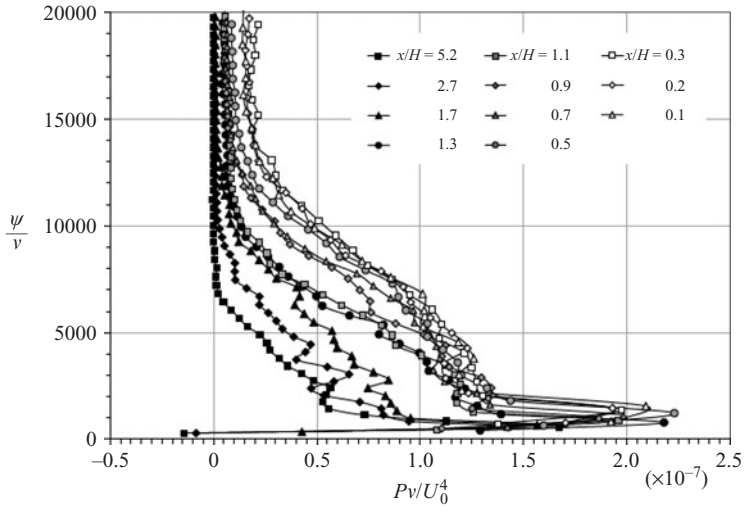


FIGURE 21. Turbulent kinetic energy production *vs.* streamfunction for different locations along the channel. Data are normalized by the kinematic viscosity and free-stream velocity at $x/H = 5.2$.

expected. The salient point is that organized turbulence still exists, i.e. Reynolds stress is non-zero, even where the acceleration parameter, K, is largest. The persistence of coherent turbulence approaching, and under, the partially blocked channel exit will be addressed in the following section.

Figures 21 and 22 show profiles of turbulent kinetic energy (TKE) production and dissipation, the two dominant terms in the turbulent kinetic energy transport equation. In both plots, energy terms are again non-dimensionalized using the upstream free-stream velocity, U_o, and plotted using the streamfunction coordinate, ψ/ν. Observe that the maximum value of production in each profile in figure 21 is essentially constant. This indicates that the reduction in Reynolds stress approaching the channel

https://doi.org/10.1017/S0022112007008300 Published online by Cambridge University Press

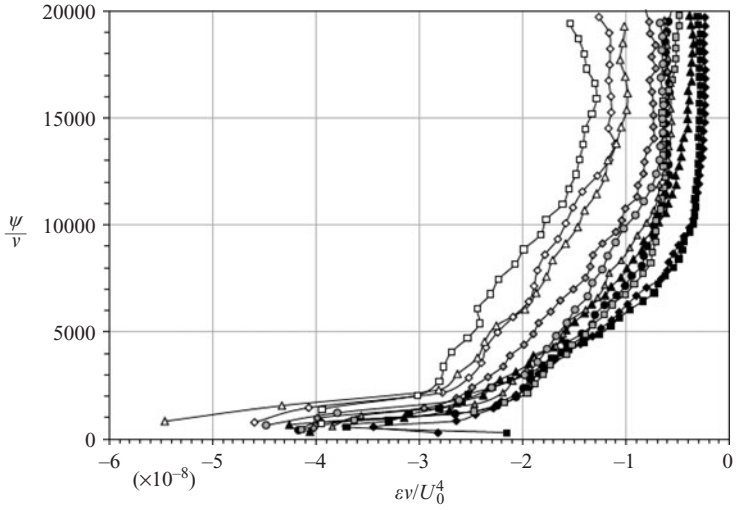


FIGURE 22. Turbulence dissipation *vs.* streamfunction for different locations along the channel. Data are normalized by the kinematic viscosity and free-stream velocity at $x/H = 5.2$.

exit is exactly offset by the higher shear. Observe also that the TKE production peak becomes broader in stream coordinates; the physical thickness of the production region is, of course, much smaller. This is consistent with the broadening of the Reynolds stress profiles shown in figure 19.

Note that turbulence dissipation, figure 16, also remains large approaching the exit. This is necessary to offset TKE production. It is noteworthy that the dissipation maximum appears to increase as x/H approaches zero. This would be consistent with the increased shear. However, spatial resolution of the measurements also decreases, making it difficult to make definitive conclusions. Finally, profiles of TKE diffusion and advection, not presented, are effectively zero across the boundary layer at all streamwise locations. There was insufficient spatial resolution, particularly at the channel exit, to resolve the diffusion and advection that must occur between the wall, where dissipation is a maximum, and the TKE production peak.

5.3. *Turbulent structure approaching the channel exit*

Examination of instantaneous velocity vector fields further illustrates changes taking place as the flow approaches and accelerates under the partial blockage. As a reference, two instantaneous velocity fields in the x, y-plane, centred at $x/H = 5.25$, are presented in figure 23(a). Flow in both fields is from left to right. Note that the local mean streamwise velocity magnitude, $U(y/H)$, has been subtracted from each velocity vector in the two fields. This is a somewhat unconventional way of plotting vector fields; one typically subtracts a single constant velocity magnitude from every vector for side-view velocity fields. However, this method of plotting simply shows the Reynolds decomposed fluctuating velocity field and is very useful for highlighting coherent structures. That is, the two vector fields in figure 23 are instantaneous snapshots of fluctuating velocity fields. Observe the coherent structures characteristic of a canonical turbulent boundary layer. Spanwise vortices, high-momentum sweeps and low-momentum ejections inclined at the angle of 45° populate the region extending from the wall to $y/H \approx 0.3$.

https://doi.org/10.1017/S0022112007008300 Published online by Cambridge University Press

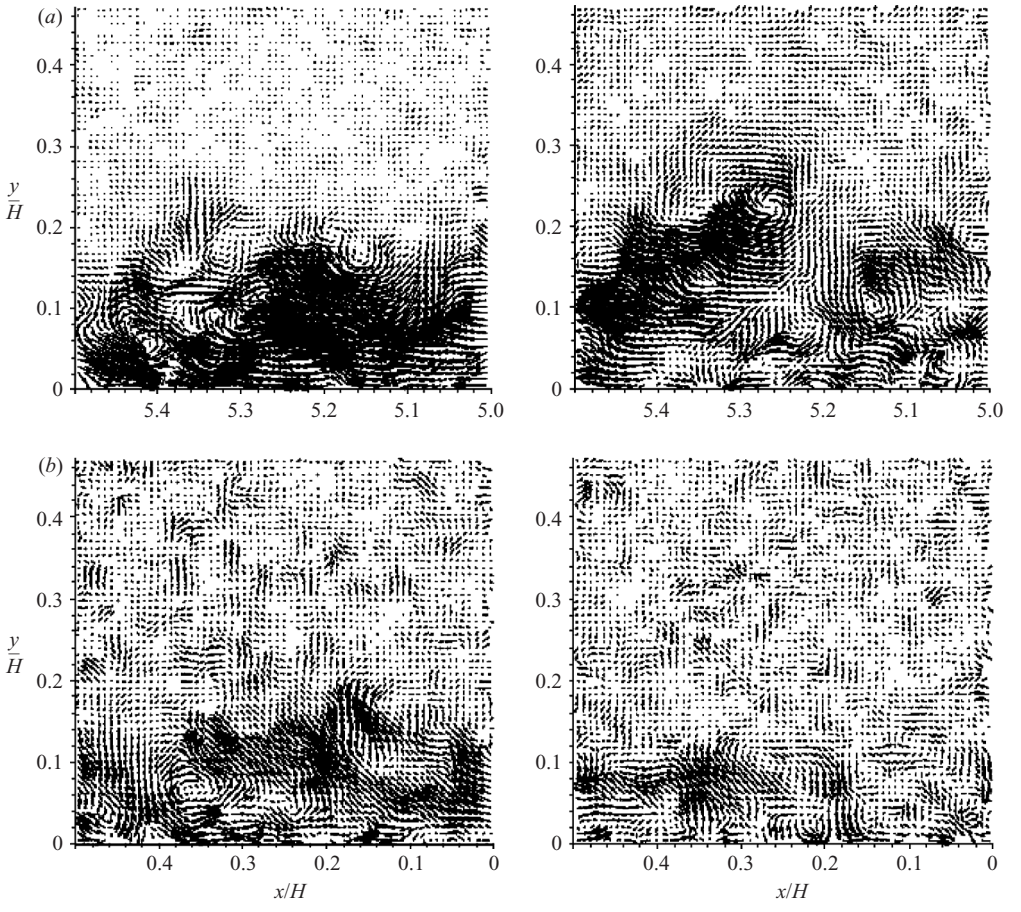


FIGURE 23. Instantaneous velocity fields in the x, y-plane at (*a*) $x/H = 5.25$, (*b*) $x/H = 0.25$.

Side-view instantaneous vector fields, centred at $x/H = 0.25$, are presented in figure 23(*b*). For these plots, the local mean streamwise velocity magnitude, $U(y/H)$, has been subtracted from every velocity vector. The acceleration parameter, K, at this location is 6.7×10^{-6}. At this position strong large-scale flow structures could be observed only very close to the wall. However, there are a number of instantaneous vector fields in which the flow appears laminar all the way to the wall. This indicates increasing intermittency even in the near-wall region. Furthermore, in other vector fields, turbulent structures appear to be relatively large in proportion to the local boundary layer thickness. These are interpreted to be remnants of structures generated upstream of the acceleration region which have not yet been fully compressed by the partial exit blockage. In this region, the DPIV sampling rate is not high enough to temporally resolve the evolution of these eddies; this is a subject that must be deferred for a later study.

Instantaneous plan-view (i.e. the x, z plane) velocity fields at two streamwise positions, $x/H \approx 5.5$ and $x/H \approx 0.5$ are shown in figures 24(*a*) and 24(*b*), respectively. The local mean streamwise velocity has again been subtracted from every vector.

In figure 24(*a*), the upstream cases at $x/H \approx 5.5$, the measurement plane was located at $y/H = 0.06$ corresponding to $\psi = 2000$ (or $y^+ \approx 150$). The vector field in figure 24(*b*) is located at $y/H = 0.02$, corresponding to $\psi = 1500$ (or $y^+ \approx 120$). The wall-normal

https://doi.org/10.1017/S0022112007008300 Published online by Cambridge University Press

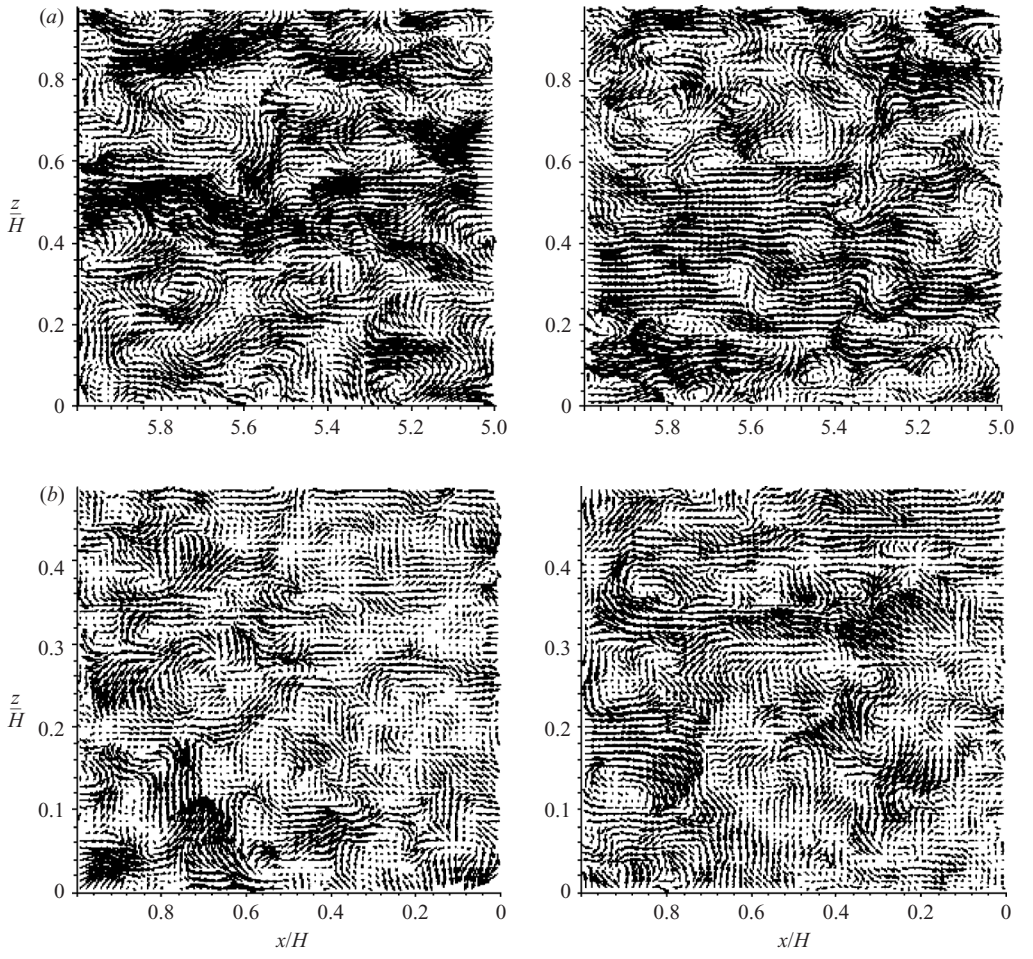


FIGURE 24. Instantaneous velocity fields in the x, z-plane at (*a*) $x/H = 5.5$, $y/H = 0.06$; (*b*) $x/H = 0.5$, $y/H = 0.02$.

locations in figures 24(*a*) and 24(*b*) were intentionally selected so that one can see the development of flow structures along approximately constant streamfunction values.

In figure 24(*a*), large, coherent, streamwise low-speed streak-like structures populate the field of view. These can be identified as nominally horizontal bands of velocity vectors pointing to the left, i.e. negative streamwise velocity fluctuations. At this location, $x/H \approx 5.5$, one channel exit opening height, H, corresponds to 2500 viscous lengths, l^+. Thus, the transverse spacing between the streaks is $500l^+ - 1000l^+$ and the streamwise extent is $2000l^+$ or more. These structures are clearly present in figure 24(*b*) as well, albeit not as strong. The salient point in comparing figures 24(*a*) and 24(*b*) is that the turbulent structures persist even in the region where the acceleration parameter, K, is nominally much larger than the relaminarization limit.

5.4. *Thoughts on relaminarization and the acceleration parameter*

There are many similarities between the turbulent boundary statistics presented in this paper and those presented by Blackwelder & Kovasznay (1972) and Escudier *et al.* (1998). All three studies clearly show, for example, the effect of decreasing boundary layer thickness in response to strong acceleration. There are, however, distinct and

https://doi.org/10.1017/S0022112007008300 Published online by Cambridge University Press

important differences between the three investigations. Blackwelder & Kovasznay (1972) reported that the boundary layer they studied thinned significantly only after K reached the threshold level of 3×10^{-6}. Escudier *et al.* (1998), however, found in their experiment that boundary layer thinning started well before K reached this threshold. In contrast to the other two studies, the present experiments show that the outer edge of the boundary layer follows a constant streamfunction, i.e. a single streamline, all the way to the partially blocked channel exit; both Blackwelder & Kovasznay (1972) and Escudier *et al.* (1998) observed that even using stream coordinates, the boundary layer thickness decreases with increasing acceleration.

The acceleration parameter, K, was defined to establish a criterion for predicting the onset of relaminarization. However, the results of this investigation coupled with the work of Blackwelder & Kovasnay (1972) and Escudier *et al.* (1998), clearly indicate that K is, at best, and incomplete indicator. This is most obvious when considering the fact that the boundary layer remains turbulent along the entire channel length. This is true even where $K_{max} \approx 6.75 \times 10^{-6}$. Recall that K_{max} is more than twice the nominal relaminarization limit of 3×10^{-6}. The turbulence intensity profiles, figures 14–16, Reynolds stress data, figures 18–20, TKE production profiles, figure 21, and the instantaneous vector fields, figures 24–26, all show clear evidence of turbulence at high values of K.

It should be noted in closing that there are unique features of the present study which may separate it from other relaminarization studies. One of the first distinctions is that a quasi-laminar state cannot be readily distinguished in the mean velocity profiles. Indeed, Sreenivasan (1982) pointed out that during relaminarization, the mean velocity profile need not approach the canonical laminar Blasius shape. It is possible that in the present setup, for instance, the typical characteristics of a laminar profile may have been masked by distortions in the mean-flow pattern as flow approaches the partially blocked exit. The wall-normal profiles in the most downstream locations are strongly affected by the contraction, i.e. maxima of the velocity profiles approaching the channel exit lie closer to the bottom wall than the top of the exit, which is the bottom edge of the partial blockage. Thus, there is an inherent asymmetry associated with the acceleration in the present study that is typically not present in other studies. This may account for discrepancies observed between this and other research on relaminarization. Nonetheless, the present results clearly show that the threshold acceleration parameter, $K = 3 \times 10^{-6}$ is not relevant to this problem.

6. Conclusions

In this investigation, turbulent boundary layer flow through a rectangular channel terminated with a partial blockage on the top wall has been studied. The addition of a partial blockage at the exit of a nominally laminar duct flow results in high degrees of turbulence immediately upstream and past the blockage. Coherent structures associated with this flow include an unsteady spanwise vortex in the corner upstream of the blockage, and counter-rotating streamwise vortices flowing past the blockage.

The results presented in this study show that the strong favourable pressure gradient generated by the partial blockage tends to significantly attenuate the turbulent boundary layer on the opposing bottom wall. As a result, significant alterations to the structure of turbulence inside the boundary layer were observed. However, the flow was never observed to become fully laminar, i.e. the turbulent boundary layer never relaminarized. This leads to the key conclusion that either the acceleration parameter,

https://doi.org/10.1017/S0022112007008300 Published online by Cambridge University Press

K, is not adequate in its present form to predict the onset of relaminarization, or the nominal relaminarization threshold, $K = 3 \times 10^{-6}$, is not correct. This conclusion should be tempered with the caveat that inherent asymmetries resulting from the partially blocked channel exit geometry may account for differences between the present work and other published research on relaminarization.

Support from Metso, Inc. through Mr Hannu Lepomäki and from TEKES through Mr Reijo Munther is gratefully acknowledged. We are also indebted to Dr Ari Kiviranta for initiating this collaboration.

REFERENCES

Badri Narayanan, M. A. & Ramjee, V. 1969 On the criteria for reverse transition in a two-dimensional boundary layer. *J. Fluid Mech.* **35**, 225.

Blackwelder, R. F. & Eckelmann, H. 1979 Streamwise vortices associated with the bursting phenomenon. *J. Fluid Mech.*, **94**, 577.

Blackwelder, R. F. & Kovasznay, L. S. G. 1972 Large-scale motion of a turbulent boundary layer during relaminarization. *J. Fluid Mech.* **53**, 61.

Brown, G. L. & Roshko, A. 1974 On density effects and large structure in turbulent mixing layers. *J. Fluid Mech.* **64**, 775.

Eloranta, H. 2000 Near-wall coherent flow structures in the papermachine headbox slice. MS Thesis, Tampere University of Technology.

Eloranta, H. 2005 Fluid mechanics of the papermaking machine headbox – instabilities and disturbances in the slice chamber. PhD. Dissertation, Institute of Energy and Process Engineering, Tampere University of Technology, Finland.

Escudier, M. P., Abdel-Hameed, A., Johnson, M. W. & Sutcliffe, C. J. 1998 Laminarisation and re-transition of a turbulent boundary layer subjected to favourable pressure gradient. *Exps. Fluids* **25**, 491.

Fernholz, H. H. & Warnack, D. 1998 The effects of a favourable pressure gradient and of the Reynolds number on an incompressible axisymmetric turbulent boundary layer. Part 1. The turbulent boundary layer. *J. Fluid Mech.* **359**, 329.

Görtler, H. 1940 Uber eine driedimensionale instabilität laminarer grenzschichten an konkaven wanden. *Math. Phys. Kl* **2**, 1 (also NASA TM 1375 (1954)).

Grega, L. M., Hsu, T. Y. & Wei, T. 2002 Vorticity transport in a corner formed by a solid wall and a free surface. *J. Fluid Mech.* **465**, 331.

Grega, L. M., Wei, T., Leighton, R. I. & Neves, J. C. 1995 Turbulent mixed-boundary flow in a corner formed by a solid wall and a free surface. *J. Fluid Mech.* **294**, 17.

Hsu, T. Y. 2000 Turbulent secondary flow in the mixed boundary corner formed by a horizontal free surface and a vertical solid wall. MS Thesis, Rutgers, The State University.

Hsu, T. Y. 2002 Hydrodynamics of paper making: streamwise vortices generated in upstream of a 2-D Jet Nozzle. PhD Dissertation, Rutgers; The State University of New Jersey, USA.

Hsu, T. Y., Grega, L. M., Wei, T., & Leighton, R. I. 2000 Turbulent kinetic energy transport in a corner formed by a solid wall and a free surface. *J. Fluid Mech.* **410**, 343.

Hsu, T. Y. & Wei, T. 2004 Generation of streamwise vortices in a slice knife model: Can streaks be generated at the slice exit? *TAPPI J.* **3**, 3.

Jones, W. P. & Launder, B. E. 1972 Some properties of sink-flow turbulent boundary layers. *J. Fluid Mech.* **56**, 337.

Kim, K. C. & Adrian, R. J. 1999 Very large-scale motion in the outer layer. *Phys. Fluids* **11**, 417.

Kline, S. J., Reynolds, W. C., Schraub, F. A. & Runstadler, P. W. 1967 The structure of turbulent boundary layers. *J. Fluid Mech.* **50**, 133.

Mei, R. W. & Plotkin, A. 1986 Navier-Stokes solutions for laminar incompressible flows in forward-facing step geometrices. *AIAA J.* **24**, 1106.

Morel, T. 1977 Design of two-dimensional wind tunnel contractions. *Trans. ASME: J. Fluids Engng* **99**, 371.

https://doi.org/10.1017/S0022112007008300 Published online by Cambridge University Press

Moretti, P. H. & Kays, W. M. 1965 Heat transfer in turbulent boundary layer with varying free-stream velocity and varying surface temperature – an experimental study. *Intl J. Heat Mass Transfer* **8**, 1187.

Myose, R. Y. & Blackwelder, R. F. 1991 Controlling the spacing of streamwise vortices on concave walls. *AIAA J.* **29**, 1901.

Myose, R. Y. & Blackwelder, R. F. 1994 On the role of the outer region in the turbulent-boundary-layer bursting process. *J. Fluid Mech.* **259**, 345.

Narasimha, R. & Sreenivansan, K. R. 1979 Relaminarization of fluid flows. *Adv. Appl. Mech.* **19**, 221.

Piomelli, U., Balaras, E. & Pascarelli, A. 2000 Turbulent structures in accelerating boundary layers. *J. Turbulence,* http://jot.iop.org/, 1/2000.

Robinson, S. K. 1991 Coherent motions in the turbulent boundary layer. *Annu. Rev. Fluid Mech.* **23**, 601.

Rothenflue, J. A. & King, P. I. 1996 Three-dimensional velocity measurements within Görtler vortices. *AIAA J.* **34**, 1736.

Shah, P., Atsavapranee, P., Hsu, T. Y., Wei, T. & McHugh, J. 1999 Turbulent transport in the core of a trailing delta wing vortex. *J. Fluid Mech.* **387**, 151.

Shah, P. N., Atsavapranee, P., Wei, T. & McHugh, J. 2000 The role of turbulent elongational stresses on deflocculation in paper sheet formation. *TAPPI J.* **83**, 70.

Sherman, F. S. 1990 *Viscous Flow*. McGraw-Hill.

Smith, C. R. & Schwartz, S. P. 1983 Observation of streamwise rotation in the near-wall region of turbulent boundary layer. *Phys. Fluids* **26**, 241.

Smith, G. B. 1992 Turbulent cascade to small scales during the off-axis collision of two vortex rings. MS Thesis, Rutgers, The State University of New Jersey.

Soderberg, L. D. & Alfredsson, P. H. 1997 Experiments concerning the creation of streaky structures inside a plane water jet. *Proc. 1997 TAPPI Engineering Conference*, p. 1205.

Spalart, P. R. 1986 Numerical study of sink-flow boundary layers. *J. Fluid Mech.* **172**, 328.

Sreenivasan, K. R. 1982 Laminarescent, relaminarizing and retransitional flows. *Acta Mech.* **44**, 1.

Swearingen, J. D. & Blackwelder, R. F. 1987 The growth and breakdown of streamwise vortices in the presence of a wall. *J. Fluid Mech.* **182**, 255.

Talamelli, A., Fornaciari, N., Westin, K. J. A. & Alfredson, P. H. 2002 Experimental investigation of streaky structures in a relaminarizing boundary layer. *J. Turbulence* http://jot.iop.org/, 3/2002, 018, 13 p.

Warnack, D. & Fernholz, H. H. 1998 The effects of a favourable pressure gradient and of the Reynolds number on anincompressible axisymmetric turbulent boundary layer. Part 2. The boundary layer with relaminarization. *J. Fluid Mech.* **359**, 357.

Wei, T. & Smith, C. R. 1986 Secondary vortices in the wake of circular cylinders. *J. Fluid Mech.* **169**, 513.

Willert, C. E. & Gharib, M. 1991 Digital particle image velocimetry. *Exps. Fluids* **10**, 181.

https://doi.org/10.1017/S0022112007008300 Published online by Cambridge University Press